Nanotechnology **20** (2009) 035701 (6pp) doi:10.1088/0957-4484/20/3/035701

Morphological work function dependence of rare-earth disilicide metal nanostructures

Sangyeob Lee[1], **Aniketa Shinde**[1,2] **and Regina Ragan**[1,3]

[1] Department of Chemical Engineering and Materials Science, University of California, Irvine, CA 92697, USA
[2] Department of Physics and Astronomy, University of California, Irvine, CA 92697, USA

E-mail: rragan@uci.edu

Received 27 September 2008, in final form 31 October 2008
Published 17 December 2008
Online at stacks.iop.org/Nano/20/035701

Abstract
The work functions of various $DySi_{2-x}$ nanostructures epitaxially grown on a Si(001) surface were correlated with the structure using high-resolution Kelvin probe force microscopy and scanning tunneling microscopy in ultrahigh vacuum. Dy adatoms induce a surface dipole on Si(001) that increases the surface potential from 0.26 to 0.42 eV with respect to 2×1 reconstructed Si(001). $DySi_{2-x}$ nanowires showed a 0.2–0.23 eV lower work function than $DySi_{2-x}$ nanoislands, which can be attributed to confinement of electrons along the surface normal that induces a surface dipole when the film thickness approaches the Fermi wavelength. The ability to tune the work function of metal nanostructures should be useful for understanding how electronic structure affects catalytic activity.

(Some figures in this article are in colour only in the electronic version)

1. Introduction

Rare-earth disilicides ($RESi_{2-x}$) have attracted much interest, since the material system forms various nanostructures such as nanowires (NWs) [1, 2] and nanoislands (NIs) [3, 4] when epitaxially grown on Si substrates and due to a low (high) Schottky barrier height on n-type Si (p-type Si) [5]. As dimensions in electronic devices scale toward atomic dimensions it is necessary to understand how electrical properties evolve with size and when quantum size effects (QSE) become significant. Several theoretical calculations have predicted electronic properties of low dimensional metallic systems. For example, Smogunov *et al* utilized a jellium model in the framework of density-functional theory (DFT) for metal NWs and found that the electron potential exhibited Friedel oscillations and the work function asymptotically increased to approach the bulk metal work function as the radius of NWs increased [6]. Other self-consistent DFT calculations have predicted oscillations of the work function with film thickness for thin metal films on the order of a few crystalline layers [7]. Theoretical studies provide insight into predicted behavior at the nanoscale, yet experimental realization of electrical properties as a function of nanoscale size is lacking due to difficulties of fabricating well-defined metallic structures on length scales approaching the Fermi wavelength. $RESi_{2-x}$ NWs are a model system to understand electronic properties in quantized metallic structures since disilicide nanostructures are fabricated via self-assembly in ultrahigh vacuum conditions, thus nanometer feature sizes are achievable and the pristine surface can be probed *in situ* in order to correlate morphology and electronic properties. Furthermore, $RESi_{2-x}$ nanostructure morphology can be controlled via growth conditions and thereby electronic properties can be measured as a function of feature size and film thickness. In this publication, the evolution of local electronic properties of metallic nanostructures with morphology was investigated for several different types of disilicide structures. Specifically Dy adatoms, $DySi_{2-x}$ NWs and $DySi_{2-x}$ NIs were all imaged on Si(001) substrates with scanning tunneling microscopy (STM) and atomic force microscopy (AFM) and local electronic structure was measured using Kelvin probe force microscopy (KPFM). The local electronic properties of a metal [8], especially the work function, are important factors in influencing

[3] Author to whom any correspondence should be addressed.

functional properties such as catalytic activity in heterogeneous catalysis [9].

2. Experimental details

All experiments were performed in an ultrahigh vacuum chamber with a base pressure of 7×10^{-11} Torr. The chamber is equipped with an Omicron VT AFM/STM system with an external Omicron KPFM electronics module. Clean 2×1 reconstructed Si(001) (Boron doped, 0.01–0.04 Ω cm, Virginia Semiconductor) surfaces were prepared by quickly ramping the temperature to 1150 °C, holding for 30 s with a chamber pressure less than 5×10^{-10} Torr, cooling down the sample quickly to 900 °C, and then holding at 900 °C for 5 min. Subsequently, the samples were slowly cooled to room temperature at a rate of 1–2 °C s^{-1}. Prior to deposition, the Si(001) surface was investigated with STM to confirm a 2×1 reconstructed surface state. Dy (99.9%, ESPI) was then deposited using an e-beam evaporator (Quad-EV-C, Mantis) at an emission power of 23 W for 1 min to obtain submonolayer coverage. Before Dy evaporation, Dy source and crucible were extensively out gassed in UHV to minimize contamination of the surface during evaporation. During Dy deposition, the Si(001) surface was kept at 600 °C with chamber pressure of less than 2×10^{-9} Torr. After Dy deposition, the samples were post-annealed at 680 °C for 2 min, and analyzed with STM and KPFM. In order to acquire larger NI structures, the post-growth annealing step was performed at 800 °C for 30 min and structures were also analyzed with STM and KPFM. In both cases, the samples were allowed to cool down to room temperature before imaging. In order to obtain high lateral resolution, KPFM and topographic AFM imaging were performed in frequency modulation mode [10–12] using super sharp silicon tips (typical tip radius less than 2 nm, Nanosensors). KPFM has the capability to simultaneously image topography and contact potential difference (CPD) between the surface and the probe with atomic resolution [10]. Si AFM tips were coated with approximately 3 nm of Cr using an Ar sputtering system (IBS, Southbay Technology) to obtain a conducting tip for KPFM analysis. The resonance frequency of the tip was measured as 270.9 kHz and the nominal spring constant was listed as 30 N m^{-1}. The AFM cantilever was oscillated at the resonance frequency and with constant amplitude of 7.3 nm.[4] At the same time, 2 V_{pp} with 2 kHz ac voltage was applied to the tip in order to measure CPD between tip and the sample.

CPD is defined as

$$\mathrm{CPD} = \frac{\phi_{\mathrm{tip}} - \phi_{\mathrm{sample}}}{-e} = \pm V_{\mathrm{ext}}, \qquad (1)$$

where, ϕ_{tip} and ϕ_{sample} are the work function of the tip and the sample, respectively, e is the electron charge, and V_{ext} is the applied external voltage. The sign of V_{ext} is determined by whether the external bias is applied to the sample (+) or the tip (−) [13]. In our experimental setup the voltage is applied to the tip, so that the sign on V_{ext} is (−) and thus an increase in CPD corresponds to a lower work function of the sample when the same tip is used. In all sample analysis, topography and CPD images were acquired simultaneously at room temperature using the same Cr-coated Si AFM tip.

[4] Calculated amplitude given the geometry of the Omicron VT AFM system using the following equation:

$$A_{\mathrm{phys}} = 2 l_{\mathrm{CL}} \tan\left(\frac{A_{\mathrm{PSD}}}{52 I_{\mathrm{tot}}}\right)$$

A_{phys}: physical amplitude (nm); A_{PSD}: position sensitive detector amplitude (V); l_{CL}: cantilever length (nm); I_{tot}: total position sensitive detector intensity (V).

3. Results and discussion

Figures 1(a) and (b) show STM images of Dy deposited on Si(001) with similar coverage (deposition for 1 min with an emission power of 23 W) and sample growth temperature (600 °C) but different post-growth annealing conditions; (a) 680 °C for 2 min, and (b) 800 °C for 30 min. As seen in the STM image of the sample shown in figure 1(a), $DySi_{2-x}$ NWs are observed along $\langle 1\bar{1}0 \rangle$ on Si(001) and some rectangular shaped NIs (thin-NIs) are also formed along $\langle 1\bar{1}0 \rangle$ that typically intersect NWs. As annealing temperature is increased to 800 °C, larger NIs (thick-NIs) with square and rectangular shapes form as observed in the STM image of figure 1(b). Representative line profiles of NIs taken across the lines in figures 1(a) (labeled 1) and (b) (labeled 2) are shown in figures 1(c) and (d), respectively. Thin-NIs have heights less than 3 nm and thick-NIs have heights greater than 4 nm; hence the name designation. It has been previously reported that the crystal phase of $RESi_{2-x}$ varies with nanostructure morphology on Si(001) surfaces [3, 4, 13]. It is important to clarify the crystal structure of each nanostructure since metal work functions, and thereby the measured CPD values, may vary with crystal structure. The feature height of the thin-NI in the line profile of figure 1(c) is measured as 0.98 nm and is an integral multiple of the height of one unit cell along $[1\bar{1}00]$ of $DySi_{2-x}$ in the hexagonal AlB_2 crystal structure (0.33 nm) [4]. We have measured 24 different step heights of thin-NI, and the mean value of features was 0.97 nm with a measurement error of approximately 10%. The measured height values of thin-NI are thereby not consistent with the length of the unit cell along the Si(001) surface normal (c axis = 1.338 nm) if the island was in the tetragonal phase [14]. In contrast, the line profile of the thick-NI shows a feature height of 4.06 nm which is approximately three times the lattice parameter of the tetragonal phase of $DySi_{2-x}$ along the c axis. The tetragonal structure is also evident from the surface reconstruction of the thick-NI shown in the inset in figure 1(b). From this analysis, one can conclude that thick-NIs exhibit the tetragonal crystal structure and thin-NIs exhibit the hexagonal AlB_2-type crystal structure as is the reported crystal phase of NWs having height of less than or equal to four monolayers [3, 14]. In order to determine if the feature heights measured via STM are significantly influenced by electronic structure, the STM measured feature heights of thick-NI were compared with AFM measurements and found to be consistent.

Figure 2 shows high-resolution STM images of the Si(001) surface adjacent to (a) a NW after 680 °C post-growth annealing and (b) a thick-NI after 800 °C post-growth annealing. In the case of figure 2(a), a Dy induced $(2 \times n)$

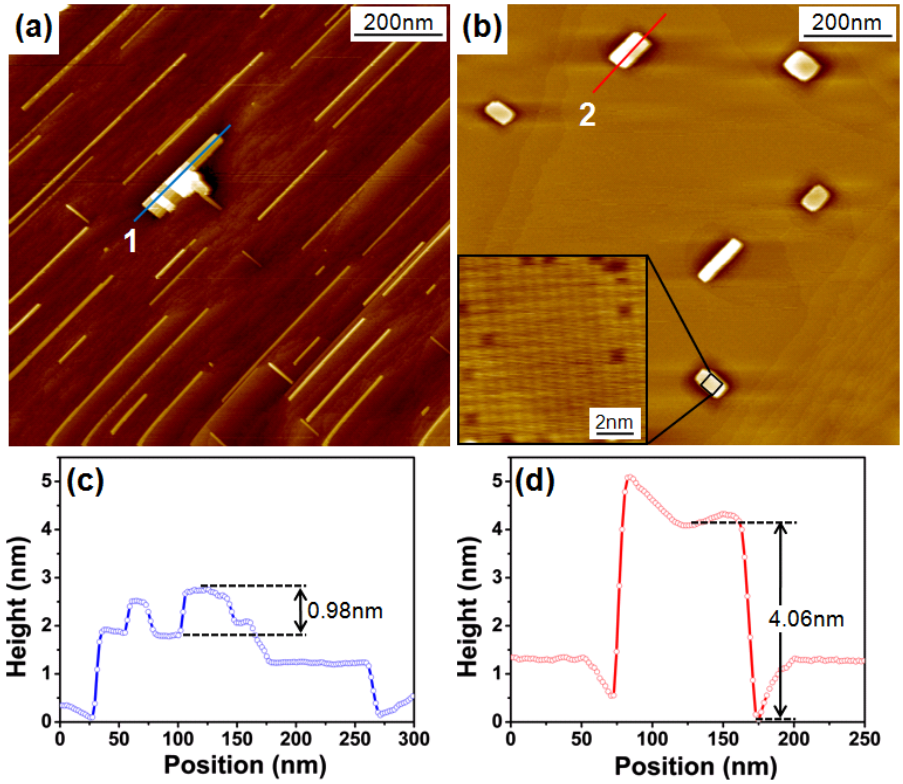

Figure 1. 1 μm $\times$ 1μm STM images of $DySi_{2-x}$ nanostructures on Si(001) surfaces: (a) post-growth annealed at 680 °C for 2 min and (b) post-growth annealed at 800 °C for 30 min. Inset in (b) shows 10 nm $\times$ 10 nm atomic resolution image of the surface of a thick-NI. Line profiles across lines of a thin-NI, labeled 1 in (a), and thick-NI, labeled 2 in (b), are shown in (c) and (d), respectively. (Sample bias: -2.0 V, feedback current: 0.2 nA for all STM images.)

surface reconstruction is observed on Si(001) that indicates the presence of Dy surface adatoms [15]. In comparison, Si dimer rows are more visible and ordered in figure 2(b) thereby indicating a lower coverage of Dy adatoms than shown in figure 2(a) since at higher annealing temperatures Dy adatoms are consumed in nanostructure formation. From the high-resolution STM images of figures 2(a) and (b), we did not observe significant evidence of absorbed contaminant on the surface during Dy deposition. KPFM CPD values of a sample after 600, 680 and 800 °C post-growth annealing were measured to quantify the effect of a Dy induced $(2 \times n)$ reconstructed Si(001) surface, i.e., Dy adatoms, on surface potential. Prior to Dy deposition, KPFM analysis measured an average CPD of $-1.03 \pm 0.03(1\sigma)$ eV on a clean 2×1 reconstructed Si(001) and the data is shown in the CPD histogram (open purple circles) of figure 2(c). Also shown in figure 2(c) are measured CPD values after Dy deposition as a function of annealing temperature. The mean CPD of the sample after 600 °C post-growth annealing was $-0.61 \pm 0.05(1\sigma)$ eV (closed blue triangles), after 680 °C post-growth annealing was $-0.77 \pm 0.04(1\sigma)$ eV (open red triangles) and after 800 °C post-growth annealing was $-0.97 \pm 0.04(1\sigma)$ eV (closed green circles). According to equation (1), when two measured CPD values using the same tip are compared, the higher measured CPD value is associated with a lower work function (higher surface potential), since the tip work function is constant. Thus, from the histograms of figure 2(c) the surface potential decreases as the annealing temperature increases. Since, as mentioned prior, Dy adatom coverage decreases with increased annealing temperature, the surface potential decreases as Dy adatom coverage decreases. DFT calculations predict charge transfer from Dy adatoms to Si due to differences in electronegativity between Si(1.9) and Dy (1.2) [16] resulting in a surface dipole that is oriented along the surface normal. The predicted Dy adatom induced dipole increases the surface potential, and this is consistent with the higher CPD values obtained in the KPFM measurement for the sample annealed at 600 and 680 °C versus that of the sample annealed at 800 °C. The measured CPD after annealing at 800 °C is close to the measured CPD value of a 2×1 reconstructed Si(001) substrate. This lower surface potential is correlated with a lower coverage of Dy adatoms since the surface exhibits a 2×1 reconstructed surface due to incorporation of Dy adatoms into larger NIs as shown in figure 2(b).

KPFM analysis was also performed on the three different $DySi_{2-x}$ nanostructures on Si(001), NWs, thin-NIs, and thick-NIs, that are represented in figure 1. Figure 3 shows KPFM measurements of (a) topography and (b) CPD of $DySi_{2-x}$ NWs and a thin-NI that result from the 680 °C post-growth annealing step and (c) topography and (d) CPD of $DySi_{2-x}$ thick-NIs formed after 800 °C post-growth annealing. All KPFM measurements were performed using the same Cr-coated AFM tip and therefore all CPD values have the same reference point.

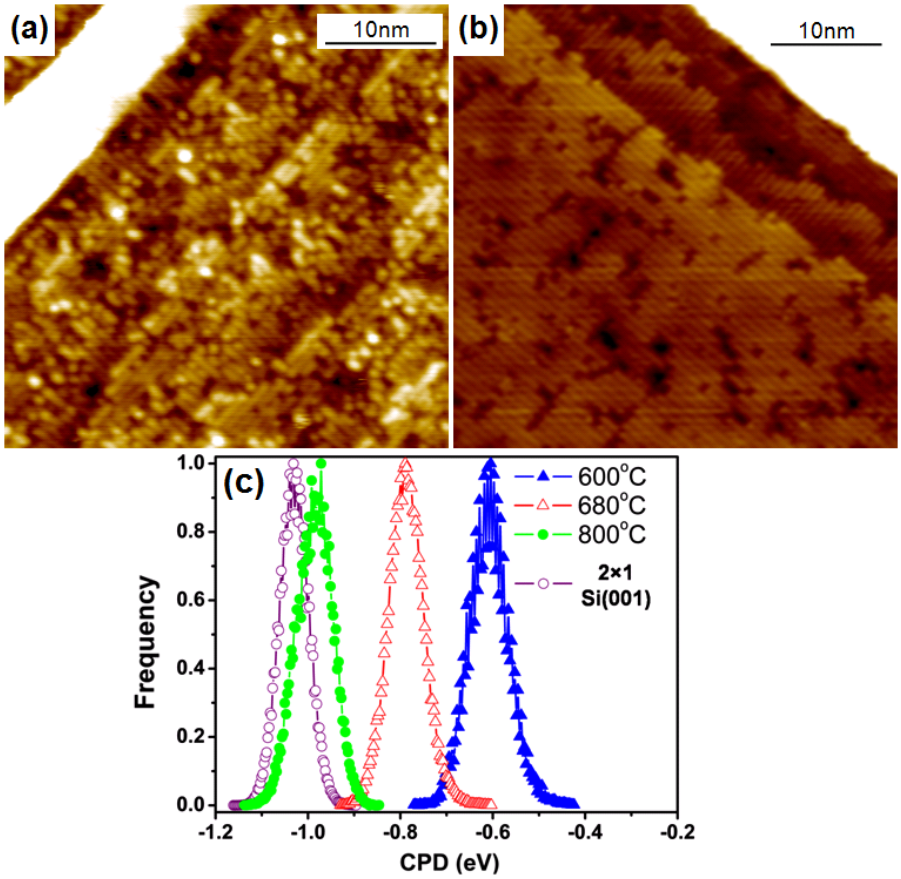

Figure 2. 40 nm × 40 nm high-resolution STM images of the Si(001) substrate in the vicinity (a) of a NW that was also shown in figure 1(a), and (b) of a thick-NI that was also shown in figure 1(b). (Sample bias: −2.0 V, feedback current: 0.2 nA for all images.) (c) Histograms of measured CPD values of 2 × 1 reconstructed Si(001) (open purple circles) and Si(001) substrate in the vicinity of NW and/or NI after post-growth annealing at 600 °C (closed blue triangles), 680 °C (open red triangles), and 800 °C (closed green circles).

Thus, the correlation between work function and structure can clearly be seen in the simultaneous topography and CPD line profiles of a NW, a thin-NI and a thick-NI that are shown in figures 3(e), (f) and (g), respectively. There are several observations to discuss. First note that the surface potential of the Si(001) substrate in between nanostructures and therefore CPD of the background varies with annealing temperature due to differing coverage of Dy adatoms as quantified in figure 2(c). One also observes an increase in CPD along NI feature edges in both thin-and thick-NI in comparison to the interior. This CPD increase can be explained by a decrease of the work function due to the presence of dipoles at step edges of a metallic surface [11, 17, 18]. The edges along NI consist of several atomic steps and the step density will be dependent on the slope at the edge of the feature and thereby feature height. The decrease of the work function associated with step edges is also known to be dependent on the step density. For example, it has been shown for Pt(111) that when the step density increases from 2×10^6 to 4×10^6 cm^{-1}, the work function decreases by 150 meV [18]. This is consistent with the KPFM data of the two types of $DySi_{2-x}$; an increase in CPD is associated with a higher relative feature height (increased step density) on the same NI and is clearly observed in both figures 3(f) and (g) by examining the line profiles on the right and left side of the NIs. In comparison, NWs appear to have a CPD value similar to that observed on the step edges of both thin-NI and thick-NI but different from the CPD values of the NI interior as observed in the CPD images shown in figures 3(b) and (d).

In order to more clearly convey the morphological dependence of the work function, statistical analysis was performed over thousands of data points for all KPFM measurements on $DySi_{2-x}$ nanostructures. Figure 4 displays histograms of measured CPD values for different $DySi_{2-x}$ nanostructures on Si(001) as well as the CPD distribution of clean 2 × 1 reconstructed Si substrate before Dy deposition as a reference. The measured CPD values of NWs was $-0.50 \pm 0.04(1\sigma)$ eV (closed blue triangles), of thin-NIs was $-0.73 \pm 0.03(1\sigma)$ eV (open red triangles) and of thick-NIs was $-0.76 \pm 0.02(1\sigma)$ eV (closed green circles). First, from the statistical analysis shown in figure 4 one can conclude that the mean CPD of thick-NIs (closed green circles) was slightly lower than that of thin-NIs (open red triangles) which means the work function of thick-NIs is slightly larger than that of thin-NIs. This small, nearly insignificant, measured change in work function can be attributed to the difference in crystal structure between the two materials that affects, e.g., surface atomic density or step density. Overall, the data indicates that the work function of $DySi_{2-x}$ does not strongly depend on

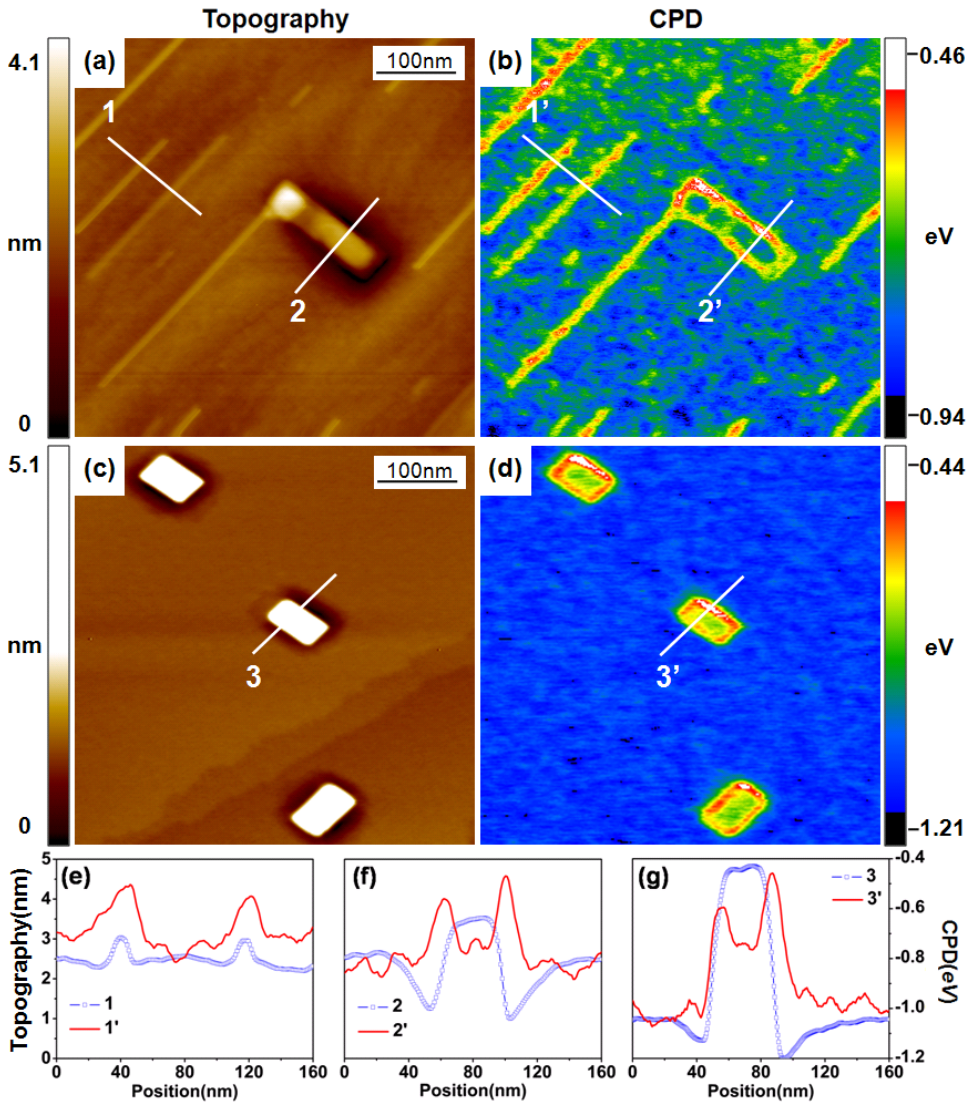

Figure 3. KPFM measurements over 500 nm × 500 nm regions of self-assembled $DySi_{2-x}$ nanostructures on Si(001) showing simultaneous (a) topography and (b) CPD after post-growth annealing at 680 °C and (c) topography and (d) CPD after post-growth annealing at 800 °C. Topography (CPD) line profiles, blue open circles (red lines), across white lines in images of the NW in (a) are labeled 1 (1′) and shown in (e), of the thin-NI in (a) are labeled 2 (2′) and shown in (f), and the thick-NI in (c) are labeled 3 (3′) and shown in (g), respectively. Note: white lines in topography and CPD images are taken along the same region.

crystal structure. From figure 4 one can also observe the CPD difference between NWs and NIs. The mean CPD value of NWs is measured as 0.2–0.23 eV higher than that of the interior of both types of NIs on average, thus the work function of NWs is lower than that of NIs. One may conclude the CPD increase is due to dipoles on step edges of NWs and this dominates the CPD values. However, the decrease in work function (CPD increase) due to dipoles along step edges is expected to be larger for NIs than NWs, since the step density (feature height) is much higher in NIs than NWs; yet the mean CPD values of the NW are comparable to those at the feature edges of NIs. The lower work function of NWs than that of the interior of NIs cannot only be attributed to dipoles along step edges but is also attributed to QSE since the average height of NWs is measured as approximately 0.7 nm corresponding to only two unit cells. QSE due to confinement of electron motion along the surface normal direction are expected to manifest when the feature size approaches the Fermi wavelength. YSi_2 has an electronic structure similar to $DySi_{2-x}$ [19, 20], and this system exhibits charge-order fluctuations in NWs having a width of 1.15 nm while NWs with a width of 1.92 nm do not [21]. This indicates that QSE will be exhibited in $DySi_{2-x}$ nanostructures having features sizes near 1 nm. Our STM and AFM height analysis of $DySi_{2-x}$ nanostructures showed that the $DySi_{2-x}$ NW heights range from 0.4 to 1.2 nm and $DySi_{2-x}$ NI heights range from 3 to 5 nm. Consequently, we expect that electron motion along the surface normal of a NW is quantized, whereas electron motion along the surface normal of a NI is not, and this is hypothesized to lead to the differing values of work function between a NW and NI. Theoretical calculations predict that the electron density distribution along the surface normal of a thin metal film varies with film thickness when the film thickness is comparable to Fermi wavelength. Thus, a dipole of varying magnitude

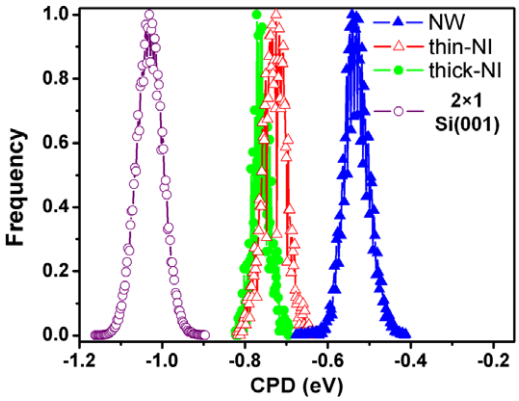

Figure 4. Histograms of measured CPD values of substrate and $DySi_{2-x}$ nanostructures on Si(001); 2×1 reconstructed Si(001): open purple circles, NW: closed blue triangles, thin-NI: open red triangles, and thick-NI: closed green circles.

is created near the surface with an orientation that oscillates parallel to anti-parallel with the surface normal with increasing film thickness leading to a work function variation (decrease to increase, respectively) as a function of film thickness. The variation of the work function with film thickness diminishes and approaches the bulk value as the film thickness approaches about four times the Fermi wavelength [7, 22]. In another self-consistent DFT calculation using the jellium model, the work function of metal NWs was also predicted to fluctuate while in this geometry the value asymptotically increases to approach the bulk metal work function as the radius of the NWs increases [6]. By comparing these theoretical studies to our experimental data, the observation that $DySi_{2-x}$ NWs have a lower work function than $DySi_{2-x}$ NIs can be attributed to electron motion confinement along the NW thickness since this dimension is comparable to the Fermi wavelength.

4. Conclusion

In conclusion, we have demonstrated a correlation between work function and nanostructure morphology. A comprehensive analysis of the surface potential of Dy adatoms on Si(001) and the work function of self-assembled $DySi_{2-x}$ nanostructures was performed by combining STM and KPFM. Dy adatoms on Si(001) induce a surface dipole, and thus exhibit a higher surface potential than clean 2×1 reconstructed Si(001). For $DySi_{2-x}$ nanostructures, the work function evolves as $\phi_{\text{thick-NI}} \geqslant \phi_{\text{thin-NI}} > \phi_{\text{NW}}$. Feature edges along NIs showed a lower work function than NIs' interior, and this is explained by the formation of dipoles along metal step edges. $DySi_{2-x}$ NWs showed a lower work function compared to $DySi_{2-x}$ NIs, which can be attributed to electron confinement as the structure height approaches the Fermi wavelength. In summary, the work function decreases with increasing step density and decreasing size of metal nanostructures. Our analysis confirms theoretical predictions of size effects in metal systems that have not been well quantified previously due to difficulties in obtaining layer-by-layer growth of metal films on length scales approaching the Fermi wavelength and performing electronic structure analysis on such pristine metal surfaces. This size dependence provides insights in the ability to vary metal nanostructure work functions and in the future correlate that with catalytic reaction rates for applications in heterogeneous catalysis.

Acknowledgments

The authors acknowledge the Donors of the American Chemical Society Petroleum Research Fund for partial support of this research and the National Science Foundation CBET-0731349 & CBET-0642217. The authors would like to thank Dr Sung-Soo Bae for helping with experimental equipment.

References

[1] Preinesberger C, Vandre S, Kalka T and Dahne-Prietsch M 1998 *J. Phys. D: Appl. Phys.* **31** L43
[2] Chen Y, Ohlberg D A A, Medeiros-Ribeiro G, Chang Y A and Williams R S 2000 *Appl. Phys. Lett.* **76** 4004
[3] Zhu Y, Zhou W, Wang S H, Ji T, Hou X Y and Cai Q 2006 *J. Appl. Phys.* **100** 114312
[4] Liu B Z and Nogami J 2003 *J. Appl. Phys.* **93** 593
[5] Tu K N, Thompson R D and Tsaur B Y 1981 *Appl. Phys. Lett.* **38** 626
[6] Smogunov A N, Kurkina L I and Farberovich O V 2000 *Phys. Solid State* **42** 1898
[7] Schulte F K 1976 *Surf. Sci.* **55** 427
[8] Wandelt K 1997 *Appl. Surf. Sci.* **111** 1
[9] Vayenas C G, Bebelis S and Ladas S 1990 *Nature* **343** 625
[10] Kitamura S and Iwatsuki M 1998 *Appl. Phys. Lett.* **72** 3154
[11] Glatzel T, Sadewasser S and Lux-Steiner M C 2003 *Appl. Surf. Sci.* **210** 84
[12] Albrecht T R, Grutter P, Horne D and Rugar D 1991 *J. Appl. Phys.* **69** 668
[13] Shikler R, Meoded T, Fried N, Mishori B and Rosenwaks Y 1999 *J. Appl. Phys.* **86** 107
[14] He Z A, Smith D J and Bennett P A 2004 *Phys. Rev.* B **70** 241402
[15] Liu B Z and Nogami J 2001 *Surf. Sci.* **488** 399
[16] Shinde A, Cao J, Lee S, Wu R and Ragan R 2008 *Chem. Phys. Lett.* at press doi:http://dx.doi.org/10.1016/j.cplett.2008.10.040
[17] Smoluchowski R 1941 *Phys. Rev.* **60** 661
[18] Besocke K, Krahlurban B and Wagner H 1977 *Surf. Sci.* **68** 39
[19] Magaud L, Veuillen J Y, Lollman D, Tan T A N, Papaconstantopoulos D A and Mehl M J 1992 *Phys. Rev.* B **46** 1299
[20] Rogero C, Koitzsch C, Gonzalez M E, Aebi P, Cerda J and Martin-Gago J A 2004 *Phys. Rev.* B **69**
[21] Zeng C, Kent P R C, Kim T H, Li A P and Weitering H H 2008 *Nat. Mater.* **7** 539
[22] Feibelman P J and Hamann D R 1984 *Phys. Rev.* B **29** 6463